



# Influence and compensation of the stator flux on the direct flux control sensorless technique for PMSMs

Emanuele Grasso<sup>1</sup>  | Marco Palmieri<sup>2</sup>  | Riccardo Mandriota<sup>1</sup> | Gianvito Gallicchio<sup>2</sup> | Francesco Cupertino<sup>2</sup> | Matthias Nienhaus<sup>1</sup>

<sup>1</sup> Lehrstuhl für Antriebstechnik, Universität des Saarlandes, Saarbrücken, Germany

<sup>2</sup> Dipartimento di Ingegneria Elettrica e dell'Informazione, Politecnico di Bari, Bari, Italy

## Correspondence

Emanuele Grasso, Lehrstuhl für Antriebstechnik, Universität des Saarlandes, Campus, Geb. E29, 66123, Saarbrücken, Deutschland.  
Email: [grasso@lat.uni-saarland.de](mailto:grasso@lat.uni-saarland.de)

## Abstract

Several techniques exploiting machines anisotropies have been proposed in literature for sensorless control of synchronous machines. Among them, the direct flux control (DFC) technique allows estimating the electrical rotor position by exploiting the zero-sequence voltage of the machine. This work aims at analysing the effects of magnetic saturation on the application of the DFC technique to permanent magnet synchronous machines. This effect is present when stator flux is controlled during machine operation, leading to an error in the estimation of the electrical rotor position. Starting from an analytical model of the machine phase inductances, a complete mathematical description of the DFC technique is derived and presented. The proposed mathematical model shows how the estimated electrical rotor position is biased when operating under load conditions. Moreover, the result of the analysis of the DFC technique allows to refine the obtained estimate and to reduce the electrical rotor estimation error. Experimental results on a test motor are provided in order to verify and support the proposed mathematical model and technique.

## 1 | INTRODUCTION

Synchronous machines (SMs) have found wide application in several fields, such as industrial, automotive, domestic. In particular, permanent magnet synchronous motors (PMSMs) represent an always more adopted solution given their high torque density and enhanced dynamic performance [1]. Nevertheless, such machines require the electrical rotor position information in order to be operative, differently from DC machines. Moreover, in order to provide high control system performance, a high resolution position sensor is necessary, as discussed in [2]. The need for a position sensor is, especially for small machines, demanding, as it increases the size and the cost of the driving solution. For this reason, several sensorless techniques have been proposed and developed in the last decades that can overcome the need of external sensing devices. In particular, sensorless techniques for PMSMs can be classified based on the effect that they rely on for operation. The main two categories are those based on the induced back electromotive force (BEMF) and those that exploit the machine anisotropies. As it is well known, the BEMF voltage is dependent on the speed

of electrical machine. Thus, it can only operate from middle to high speeds. Differently, techniques based on the machine anisotropies have the advantage of operating also at standstill and low-speed ranges.

The first contribution to machine anisotropy based sensorless techniques was made by Schrödl in [3]. The proposed technique goes under the name of INFORM and, by injecting pulse voltages relying on a modified PWM pattern, it allows to estimate the motor reactances by measuring the current signals that are dependent on the rotor position [4]. Afterwards, Lorenz proposed a novel method based on the injection of a high-frequency rotating carries in [5]. Such carrier would induce currents whose amplitude is modulated by the rotor position. Thus, a demodulation stage that can provide the rotor position estimation based on the observed signals is necessary. In order to overcome the need for demodulation and, consequently, to reduce the required computational effort, a new technique based on the injection of an alternating carrier in the estimated rotor reference frame was proposed in [6]. In this case, a pulsating voltage vector is injected along the machine q-axis. Nevertheless, an observer is still required in order to successfully estimate the

This is an open access article under the terms of the [Creative Commons Attribution](https://creativecommons.org/licenses/by/4.0/) License, which permits use, distribution and reproduction in any medium, provided the original work is properly cited.

© 2021 The Authors. *The Journal of Engineering* published by John Wiley & Sons Ltd on behalf of The Institution of Engineering and Technology

rotor position. Alternating current injection methods proved to provide more precision and robustness compared to rotating carrier. For this reason, many works focused on alternating injection, such as [7], or on arbitrary injection schemes, such as [8–11]. All the anisotropy current based sensorless techniques present the advantage that they do not require any additional hardware to perform sensorless operation since the current sensors are usually needed to achieve a high-performance machine current control. However, in order to acquire the anisotropy signals needed for the electrical rotor position estimation, the current derivative must be evaluated. Therefore, a big problem in this class of techniques is related to the low signal-to-noise ratio especially in low-power electrical machines. In order to overcome this issue, state observation techniques [4] or extensive over-sampling [12] must be adopted leading to an increase of the computational efforts in the implementation on the microcontroller.

The techniques mentioned until now are all based on the measurement of rotor position modulated currents. Nevertheless, also voltage measurements can be adopted for sensorless operation. In fact, whenever current information is not necessary for performing torque control, a voltage-based sensorless technique can contribute to diminish the cost of the system by avoiding the usage of current sensors. This is particularly relevant in embedded drive systems applications, where miniaturization of the electronics has a very important role. Moreover, the exploitation of voltage measurements presents the advantage of a higher signal-to-noise ratio and a larger bandwidth compared to current measurements. Therefore, these techniques do not require any knowledge of the machine parameters and thus state observation techniques are not necessary in the estimation of the electrical rotor position. This leads consequently in a reduction of computational efforts in the implementation on the microcontroller. Thus, these techniques are suitable for the implementation also on low performance microcontrollers. In particular, the neutral-point or star-point voltage of a star-connected machine can be exploited to estimate the electrical rotor position. From this consideration, several techniques have been proposed. One first work was proposed in [13], where the neutral voltage is used for sensorless operation of induction machines. Moreover, an interesting contribution was provided in [14], where the authors extend the application of this technique to machines that do not have an accessible star-point. Still on induction motors, other sensorless techniques were proposed by [15], where a filter has been tuned for distinguishing between the rotor bar and the magnetic saturation effects and by [16], where the noise introduced by motor cables has been considered and reduced. In [17] a thorough comparison of sensorless techniques for induction machines is presented, that includes those techniques relying on the exploitation of the neutral point voltage. Neutral voltage based sensorless techniques have then also been proposed for synchronous machines. As an extension to the work [13], the same author proposed a first technique for permanent magnet synchronous machines (PMSMs) in [18]. Also, a different approach still based on the machine neutral voltage was published in [19] that allowed the development of a technique named direct flux

control (DFC). This method obtains the anisotropy signals by evaluating the inductance variations of a star-connected PMSM by measuring the transients of the neutral-point voltage when the machine is excited by a particular PWM-pattern. First published works about the DFC technique are [20] and [21]. Here, a practical approach to the implementation of the technique has been provided together with first results concerning the estimation of the electrical rotor position. As shown in [22, 23], the anisotropy information from which the electrical rotor position is estimated using the DFC technique is dependent on the machine design. In particular, these scientific works point out that each PMSM presents different anisotropy signals in dependence of the geometry and the arrangement of the permanent magnets, the windings configuration and the pole-slot setup. Therefore, the machine design influences directly the estimated sensorless electrical position. Nevertheless, in [24, 25] it has been proved that high-efficiency performance can be obtained in driving low-power PMSMs using the aforementioned technique. In addition, these works highlight also limitations and issues in the field of applicability of the technique. Firstly, the technique is applicable only to star-connected PMSMs which present an accessible neutral-point. Consequently, an additional measurement path is necessary to perform sensorless operation. However, this restriction does not constitute a considerable limitation since in many motors the star-point is easily accessible. Moreover, the extracted anisotropy signals can be noisy due to the presence of switching electronics. To overcome this issue, low-noise electronics must be used in the measurement process of the anisotropy information. Therefore, a fast resettable integrator circuit (FRIC) capable of improving the signal-to-noise ratio of the measurements needed for the execution of the DFC technique was proposed in [26–28]. Also, the usage of a FRIC in DFC sensorless operation reduces the ringing generated by the three-phase inverter and extends the application of the technique to high-load conditions. In addition, the FRIC can be tuned in order to adapt the sensitivity of the measurements for those motors that present a weak anisotropy. The issue of noisy anisotropy signals has been also addressed in [29]. In this work a sliding mode differentiator (SMD) has been applied successfully to reduce the noise and thus to improve the electrical rotor position and speed estimation. The analyses performed on the DFC have also shown that the technique works better in the low speed range. To overcome this limitation in [30], the technique has been combined with BEMF information in order to extend the speed range also to high speed using an extended Kalman filter (EKF). Moreover, the DFC technique has been successfully used in several practical applications such as the identification of electrical and mechanical parameters of PMSMs [31] and the observation of the external load torque using state observation techniques in [32]. Besides this technique, another interesting approach was proposed by [33] that goes under the name of IVMS (induced voltage caused by magnetic saturation), that is capable of estimating the electrical rotor position by exciting two machine phases at a time and measuring the neutral point voltage. This first version of the technique was designed for brushless DC machines (BLDC), that are typically driven by means of block commutation (while Brushless

AC Machines, BLAC, rely on sinusoidal commutation). Thus, a modified version of this technique for BLAC was later on proposed in [34]. The authors show that this technique can operate also with magnetically saturated machines and, although it resembles closely the DFC technique, the utilised PWM patterns differ significantly. Both IVMS and DFC techniques rely on a measurement electronics that can be adjusted according to the electrical properties of the machine. This allows to optimise the application of the sensorless approach according to the particular machine and, therefore, also for those machines that exhibit reduced saliency variation. The modelling of the neutral point voltage is clearly fundamental for the successful development of this class of sensorless techniques. In [35], the neutral point voltage has been modelled in order to allow a prediction of its fluctuation, showing how the neutral point voltage depends on both the self and mutual inductances of the machine. Another interesting analysis of the dynamic behaviour of the neutral point voltage was provided in [28], where a full dynamic model is provided and that leads to similar conclusions to [35]. Moreover, in [36, 37] the idea of high-frequency carrier injection has been introduced also for neutral point voltage based sensorless techniques, in order, according to the authors, to increase the accuracy and the robustness of the sensorless operation for PMSMs. In both these works, an estimated reference frame rotating counterclockwise with twice the estimated electrical speed is considered and a simple demodulation algorithm is proposed. Both current and voltage based anisotropy sensorless techniques present an uncertainty of  $180^\circ$  on the estimated rotor position. In fact, it is only possible to obtain the absolute electrical rotor position for half of an electrical period. However, this issue can be overcome by means of an initialization procedure applied before starting the drive. As shown in [4, 38], this can be done by strengthening or weakening the magnetic field along the estimated d-axis revealing the actual polarity. In [39], the application of the DFC technique to PMSMs has been presented, leading to a formulation of the obtained measurements and of the estimated electrical rotor position. Moreover, it has been shown that the estimated position using this technique usually presents an error with respect to the real electrical rotor position which is related to the machine inductances matrix. Therefore, in [38] several approaches which compensate for this position estimation error have been analysed and compared. Nevertheless, an analysis of the effects of magnetic saturation has not been considered in all the aforementioned works concerning the DFC technique. This effect arises when a q-axis component of the current is commanded, leading to a further error on the estimation of the electrical rotor position. The aim of this work is to extend the mathematical description of the DFC technique including load conditions to achieve a more comprehensive description of the estimation of the electrical rotor position in the full motor operating range in the case of low-power concentrated windings PMSMs. This new formulation provides directly an approach for compensating the effects of magnetic saturation that leads to a reduction of the mean error of the estimate. After a brief recall of the DFC technique, a mathematical analysis of the quantities measured by DFC is derived by considering the machine phase inductance matrix as a

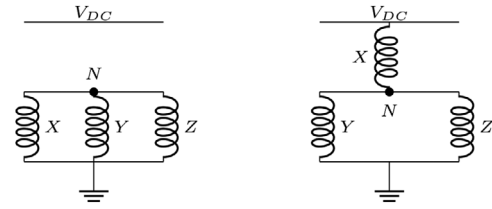


**FIGURE 1** Machine excitation states 0 (left) and I (right), where  $\{X, Y, Z\}$  represent generic phases belonging to the set  $\{A, B, C\}$

function of the stator flux. Thus, a new formulation of the DFC technique is provided as well as an extended model of the estimated electrical rotor position and its dependence on the magnetic saturation effect. The analysis leads to a compensation approach of the error introduced in the estimated electrical position. In order to validate the proposed model, experimental investigations have been carried out on a test PMSM and the obtained results are presented and discussed.

## 2 | THEORY OF THE DIRECT FLUX CONTROL

The aim of this section is to describe how the DFC technique is able to estimate the electrical rotor position starting from star-point voltage measurements and its conditions of applicability in relation with other injection methods. Also, in this section a recall of the mathematical description of the star-point voltage dynamic is reported. The DFC is an anisotropy based sensorless technique that estimates the electrical rotor position by relying on voltage measurements of the machine star-point. In particular, this technique exploits the dependence of the machine inductances on the rotor position to perform sensorless operation. This information can be obtained by measuring the zero-sequence voltage. In the case of SMs driven by a power inverter, this quantity can be obtained by measuring the difference between the star-point voltage of the machine  $v_N$  and the voltage of a virtual star-point  $v_V$  during the transition between the excitation states 0 to I. In particular, the virtual star-point is obtained by connecting the machine terminals to three resistors that are star-connected. As shown in Figure 1, during the excitation state 0 all machine terminals are grounded, while in the excitation state I, a generic phase X, belonging to the set  $\{A, B, C\}$ , switches to the inverter bus voltage  $v_{DC}$ . As presented in [28], a modified edge-aligned PWM can be used to drive the machine between the excitation states 0 and I at the beginning of each PWM period in order to allow the measurement of the differential voltage  $v_{NV}$  necessary to obtain the anisotropy signals from which the rotor position can be extracted, as shown in Figure 2. The applied PWM sequence has a time period  $T_{PWM}$  which starts in  $t_0$ . At the time instant  $t_1$ , one phase is switched to the bus voltage and then in  $t_2$  the driving edge-aligned PWM excitation is applied. In order to calculate the anisotropy signals, two measurements are performed, one per each excitation state, at the time instants  $t_{m0}$  and  $t_{m1}$ , as shown in Figure 3. It is preferable to choose  $t_{m0}$  and  $t_{m1}$  close to the switching time instant  $t_1$ . Nevertheless, it is important especially for  $t_{m1}$  to wait

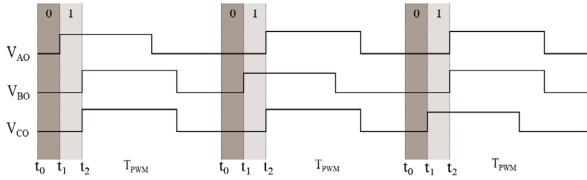


**FIGURE 2** PWM pattern used for measuring the  $v_{NN}$  voltage, where  $V_{AO}$ ,  $V_{BO}$ ,  $V_{CO}$  are the machine terminal voltages and  $O$  represents the ground reference

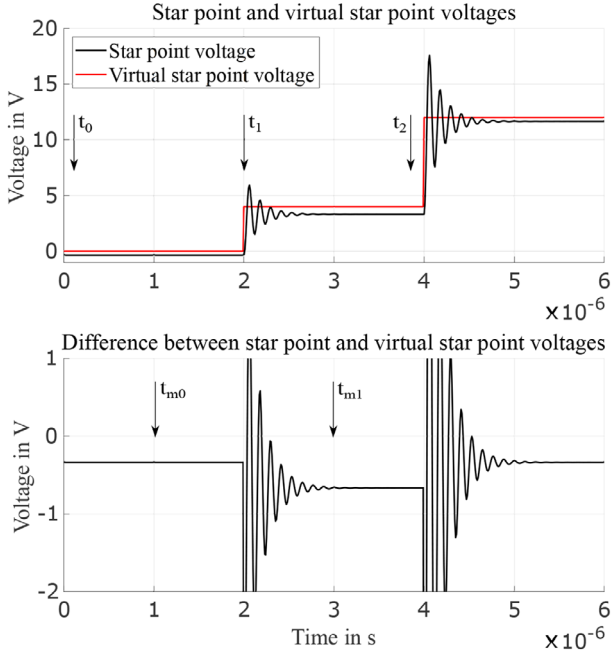


**FIGURE 3** Star-point voltages between the excitation states 0 and  $I$

for the oscillations to decay in order to reduce the disturbances on the measurements. By calculating the difference between the two measured values, a new measurement of the anisotropy signals is obtained each three PWM periods. The aforementioned measurements can be performed using voltage dividers and operational amplifiers-based voltage followers. In Figure 3, the simulated behaviour of the star-point voltages during the transition between the machine excitation states 0 and  $I$  is presented. The simulation has been performed considering the mathematical model of the star-point voltage in a star-connected PMSM with a connected measurement impedance proposed in [28].

A deeper mathematical description of the star-point voltage dynamics has been presented in [28], leading to the definition of the anisotropy signals from which the electrical rotor position can be estimated. Here in this section, a recall of this analysis is reported. Let us consider the machine electrical equation expressed in the phase reference frame:

$$\mathbf{v}_{abc}(t) = \mathbf{R}\mathbf{i}_{abc}(t) + \mathbf{L}_{abc} \frac{d\mathbf{i}_{abc}(t)}{dt}, \quad (1)$$

where  $\mathbf{v}_{abc}(t) = [v_{AN}(t) \ v_{BN}(t) \ v_{CN}(t)]^T$  and  $\mathbf{i}_{abc}(t) = [i_A(t) \ i_B(t) \ i_C(t)]^T$  are, respectively, the phase voltage and

current vectors,  $\mathbf{R}$  is the phase resistance matrix and  $\mathbf{L}_{abc}$  is the inductances matrix defined as:

$$\mathbf{L}_{abc}(\theta, \mathbf{i}_{abc}, t) = \begin{bmatrix} L_{aa} & L_{ab} & L_{ac} \\ L_{ba} & L_{bb} & L_{bc} \\ L_{ca} & L_{cb} & L_{cc} \end{bmatrix}. \quad (2)$$

It has to be remarked that the machine inductance matrix in the phase-reference frame is assumed to be non-singular, to be a function of the electrical rotor position  $\theta$  and invertible per each value of  $\theta$ . In addition, this matrix is a function of the stator currents because of the magnetic saturation effect. In fact, when the machine is loaded, the magnetization status of the stator material changes leading to a variation of the phase inductances. However, since the DFC measurements are performed within three PWM cycles, this matrix can be considered constant in the following analysis. Also, as explained in [28], within this time period the effects of the rotor speed and of the BEMF can be neglected in the machine electrical equations (1). These equations can be expressed in the Laplace domain leading to:

$$\mathbf{V}_{abc}(s) = \mathbf{R}\mathbf{I}_{abc}(s) + s\mathbf{L}_{abc}\mathbf{I}_{abc}(s). \quad (3)$$

The (3) can be written as:

$$s\mathbf{I}_{abc}(s) = \mathbf{L}_{abc}^{-1}[\mathbf{V}_{abc}(s) - \mathbf{R}\mathbf{I}_{abc}(s)]. \quad (4)$$

Since the matrix  $\mathbf{L}_{abc}^{-1} = \frac{\mathbf{L}_{abc}^*}{|\mathbf{L}_{abc}|}$ , where  $\mathbf{L}_{abc}^*$  is the adjoint matrix of  $\mathbf{L}_{abc}$  and  $|\mathbf{L}_{abc}|$  its determinant, one can write:

$$s\mathbf{I}_{abc}(s) = \frac{\mathbf{L}_{abc}^*}{|\mathbf{L}_{abc}|} [\mathbf{V}_{abc}(s) - \mathbf{R}\mathbf{I}_{abc}(s)]. \quad (5)$$

Considering a generic measurement impedance  $\zeta$  connected between the machine neutral-point and ground, the following impedance transfer function can be defined:

$$Z(s) = \frac{V_{NO}(s)}{I_{\zeta}(s)}, \quad (6)$$

where  $i_{\zeta}(t)$  is the current which flows through the measurement impedance  $\zeta$  considered positive in the direction from neutral-point to ground. In addition, the measurement impedance  $\zeta$  is supposed to be constant. Let us consider the currents Kirchoff law applied to the machine star-point in the Laplace domain:

$$\sum_{k=A,B,C} I_k(s) = I_{\zeta}(s), \quad \sum_{k=A,B,C} sI_k(s) = sI_{\zeta}(s). \quad (7)$$

Multiplying (5) on the left by the row vector  $\mathbf{T} = [1 \ 1 \ 1]$  and considering equations (6) and (7) one obtains:

$$s\mathbf{T}\mathbf{I}_{abc}(s) = \mathbf{T} \frac{\mathbf{L}_{abc}^*}{|\mathbf{L}_{abc}|} [\mathbf{V}_{abc}(s) - \mathbf{R}\mathbf{I}_{abc}(s)] = s \frac{V_{NO}(s)}{Z(s)}. \quad (8)$$



Multiplying the (8) by  $|\mathbf{L}_{abc}|$  one gets:

$$\mathbf{L}_{\Sigma_{abc}} [\mathbf{V}_{abc}(s) - \mathbf{R}\mathbf{I}_{abc}(s)] = s \frac{|\mathbf{L}_{abc}| V_{NO}(s)}{Z(s)}, \quad (9)$$

where the following row vector has been defined:

$$\mathbf{L}_{\Sigma_{abc}} = \mathbf{T}\mathbf{L}_{abc}^* = [L_{\Sigma_a} \ L_{\Sigma_b} \ L_{\Sigma_c}]. \quad (10)$$

Each element of  $\mathbf{L}_{\Sigma_{abc}}$  represents the sum of the elements of each column of the adjoint of the inductances matrix  $\mathbf{L}_{abc}^*$ . Let us express the phase voltages as the difference between the terminal voltages and the neutral-point voltage  $\mathbf{v}_{abc}(t) = \mathbf{v}_{XO}(t) - v_{NO}(t)\mathbf{T}^T$ , where  $\mathbf{v}_{XO}(t) = [v_{AO}(t) \ v_{BO}(t) \ v_{CO}(t)]^T$  are the terminal voltages. Therefore, in the Laplace domain one can write  $\mathbf{V}_{abc}(s) = \mathbf{V}_{XO}(s) - V_{NO}(s)\mathbf{T}^T$ . Consequently, the (9) can be written as follows:

$$V_{NO}(s) \left[ s \frac{|\mathbf{L}_{abc}|}{Z(s)} + \mathbf{L}_{\Sigma_{abc}} \mathbf{T}^T \right] = \mathbf{L}_{\Sigma_{abc}} [\mathbf{V}_{XO}(s) - \mathbf{R}\mathbf{I}_{abc}(s)]. \quad (11)$$

From (3) the phase currents vector  $\mathbf{I}_{abc}(s)$  can be obtained leading to:

$$\mathbf{I}_{abc}(s) = \mathbf{Z}_{abc}^{-1}(s) \mathbf{V}_{abc} = \frac{\mathbf{Z}_{abc}^*(s)}{|\mathbf{Z}_{abc}(s)|} \mathbf{V}_{abc}, \quad (12)$$

where  $\mathbf{Z}_{abc} = \mathbf{R} + s\mathbf{L}_{abc}$ ,  $\mathbf{Z}_{abc}^*(s)$  is the adjoint matrix of  $\mathbf{Z}_{abc}(s)$  and  $|\mathbf{Z}_{abc}(s)|$  its determinant. Substituting the (12) into (11) one obtains the relation between the neutral-point voltage and the applied terminal voltages:

$$V_{NO}(s) = \frac{\mathbf{N}(s)}{D(s)} \mathbf{V}_{XO}(s) = \mathbf{G}(s) \mathbf{V}_{XO}(s), \quad (13)$$

where:

$$\mathbf{M}(s) = |\mathbf{Z}_{abc}(s)| \mathbf{I} - \mathbf{R}\mathbf{Z}_{abc}^*(s), \quad (14)$$

$$D(s) = s \frac{|\mathbf{Z}_{abc}(s)| |\mathbf{L}_{abc}|}{Z(s)} + \mathbf{L}_{\Sigma_{abc}} \mathbf{M}(s) \mathbf{T}^T, \quad (15)$$

$$\mathbf{N}(s) = \mathbf{L}_{\Sigma_{abc}} \mathbf{M}(s) = [N_a(s) \ N_b(s) \ N_c(s)]. \quad (16)$$

As shown in [28], in case of a balanced three-phase machine the transfer functions  $\mathbf{G}(s) = [G_a(s) \ G_b(s) \ G_c(s)]$  are proper second-order transfer functions whose ratio between the maximum order coefficients of the polynomials are the elements of the vector:

$$\mathbf{L}_{k_{\Sigma}} = \frac{1}{\sum_{j=a,b,c} L_{\Sigma_j}} \mathbf{L}_{\Sigma_{abc}}. \quad (17)$$

The elements of  $\mathbf{L}_{k_{\Sigma}}$  represent the ratio between the sum of the elements of the  $i^{\text{th}}$  column of the matrix  $\mathbf{L}_{abc}^*$  and the sum of all its elements. Moreover, in [28] it has been shown that the presence of a measurement impedance connected to the machine neutral-point introduces a fast dynamic which does not affect the steady-state value in the neutral-point voltage dynamic. Also, this steady-state value results to be proportional to the elements of  $\mathbf{L}_{k_{\Sigma}}$ . Therefore, since the matrix  $\mathbf{L}_{abc}$  is a function of the electrical rotor position  $\theta$ , it is possible to estimate this position by measuring the elements of  $\mathbf{L}_{k_{\Sigma}}$ . These quantities can be obtained by measuring the zero-sequence voltage during the machine transitions between the excitation states 0 and I obtaining the anisotropy signals  $\mathbf{\Gamma}_{abc}$ . In [28] it has been proved that these  $\mathbf{\Gamma}_{abc}$  signals present the following expression:

$$\mathbf{\Gamma}_{abc} = \left( \mathbf{L}_{k_{\Sigma}} - \frac{1}{3} \mathbf{T} \right)^T v_{DC}. \quad (18)$$

As one can see,  $\mathbf{\Gamma}_{abc}$  contains the information related to the machine inductances from which the electrical rotor position can be extracted. As stated in [28], in order to estimate the rotor position it is convenient to transform this vector into the stator-reference frame by applying the Clarke transformation obtaining  $\mathbf{\Gamma}_{\alpha\beta\gamma}$ :

$$\mathbf{\Gamma}_{\alpha\beta\gamma} = \mathbf{T}_c \mathbf{\Gamma}_{abc}, \quad (19)$$

where  $\mathbf{T}_c$  is the Clarke transformation matrix:

$$\mathbf{T}_c = \frac{2}{3} \begin{bmatrix} 1 & -\frac{1}{2} & -\frac{1}{2} \\ 0 & \frac{\sqrt{3}}{2} & -\frac{\sqrt{3}}{2} \\ \frac{1}{2} & \frac{1}{2} & \frac{1}{2} \end{bmatrix}. \quad (20)$$

Finally, the DFC angle  $\chi$  can be obtained by applying the arctangent function as follows:

$$\chi = \arctan \left( \frac{\Gamma_{\beta}}{\Gamma_{\alpha}} \right). \quad (21)$$

A deeper analysis of the extraction of the rotor position starting from the DFC angle  $\chi$  in presence of magnetic saturation effects will be discussed in Section 3. In the following, the necessary step needed to implement the DFC technique are reported:

1. Apply a modified edge-aligned PWM excitation as shown in Figure 2 in order to let the motor switch between the machine excitation states 0 and I.
2. Measure the differential voltage  $v_{NV}$  between the machine star-point and the virtual star-point very close to the phase switching time instant  $t_1$  in  $t_{m0}$  and  $t_{m1}$  as shown in Figure 3.
3. Calculate the difference between  $v_{NV}$  evaluated in  $t_{m0}$  and  $t_{m1}$  in order to obtain the anisotropy signal  $\Gamma$  related to one phase.

4. Repeat the previous steps in order to calculate the anisotropy signals for each phase. An updated measurement of  $\mathbf{\Gamma}_{abc}$  will be obtained after three PWM periods.
5. Transform the obtained anisotropy signals  $\mathbf{\Gamma}_{abc}$  in the stator reference frame by applying the Clarke transformation obtaining the  $\mathbf{\Gamma}_{\alpha\beta\gamma}$  signals.
6. Calculate the DFC angle  $\chi$  applying (21).
7. Estimate the electrical rotor position  $\hat{\theta}$  starting from the DFC angle  $\chi$ .

Let us now discuss the conditions of applicability of the DFC technique. As shown in [39], the DFC is based on zero-sequence voltage measurements  $v_\gamma$ . It is easy to show that  $v_\gamma = -v_{NV}$ . This quantity must be not null at all time instants in order to measure the  $\mathbf{\Gamma}_{abc}$  signals. From this consideration, two equivalent applicability conditions have been obtained. The first condition relates to the machine inductances matrix expressed in the stator-reference frame  $\alpha\beta\gamma$ . In particular, the conditions  $L_{\gamma\alpha} \neq 0$  and  $L_{\gamma\beta} \neq 0$  have to be satisfied per each electrical rotor position. The second condition, instead, is that the sums of the elements of the columns of the machine inductances matrix must be not equal to each other per each electrical rotor position.

Since the DFC technique requires a modified PWM excitation, it can be considered as an injection method such as the high frequency injection (HFI) techniques. Nevertheless, the DFC exploits a different information in order to estimate the electrical rotor position compared to the quantities that are exploited by HFI methods, as stated in [40]. In fact, while the DFC technique exploits the mutual inductances  $L_{\gamma\alpha}$  and  $L_{\gamma\beta}$  in order to estimate the electrical rotor position, the HFI techniques extract information from the self-inductances  $L_{\alpha\alpha}$  and  $L_{\beta\beta}$ . Moreover, the DFC technique is based on measuring the zero-sequence voltage while HFI techniques inject carriers along the  $\alpha - \beta$  axis. Thus, although DFC is an injection technique, its conditions of applicability are strongly different from the ones of HFI methods since the zero-sequence voltage is modulated differently with respect to the electrical rotor position than the stator reference currents that are exploited by HFI techniques.

### 3 | EFFECTS OF MAGNETIC SATURATION IN DFC SENSORLESS OPERATION

In this section the effects of cross coupling magnetic saturation on star-point voltage based sensorless operation applied to low power concentrated windings PMSMs are analysed. Starting from a formulation of the machine inductances matrix which includes these effects [41], their influence on the expression of the  $\mathbf{\Gamma}_{\alpha\beta\gamma}$  signals and therefore on the rotor position estimation has been evaluated. Let us consider firstly a generic expression

of the machine inductance matrix in the phase-reference frame which considers infinite harmonic components:

$$L_{ij} = L_0 - \sum_{k=1}^{\infty} L_k \cos(k\theta + \varphi_k), \quad (22)$$

where  $L_{ij}$  is the generic element of the  $\mathbf{L}_{abc}$  matrix with  $i$  and  $j$  belonging to the set  $\{a, b, c\}$ ,  $\theta$  is the electrical rotor position,  $k$  is the order of the harmonic component,  $L_k$  is the amplitude of the  $k$ th-harmonic and  $\varphi_k$  is the corresponding phase shift. However, in some kind of machines, some harmonic components can be neglected and this expression can be simplified. According to [36, 42–48], in low power concentrated windings PMSMs, this expression can be simplified considering only the continuous component and the even harmonics of each phase inductance. In particular, the harmonics higher than the second one can be neglected since their amplitude is typically not comparable with the one of the continuous component and of the second harmonic. Thus, the following stands:

$$\begin{aligned} L_{ii} &= L_0 - L_2 \cos(2\theta + \varphi_{ii}) \\ L_{ij} |_{i \neq j} &= M_0 - M_2 \cos(2\theta + \varphi_{ij}), \end{aligned} \quad i \in \{a, b, c\} \quad (23)$$

where  $L_{ii}$  is the generic self inductance,  $L_{ij}$  is the generic mutual inductance,  $\varphi_{ij}$  is the proper phase shift of the individual phase and  $L_0$ ,  $L_2$ ,  $M_0$  and  $M_2$  are the amplitudes of the continuous and second harmonic components of the self and mutual inductances. However, the proposed model is valid only under restrictive assumptions. In fact, (23) neglects magnetic saturation effects which generate a phase shift on the inductances, as reported in [39]. Therefore, in order to take into account these effects, as proposed in [36], the following formulation of  $\mathbf{L}_{abc}$  has been considered:

$$\begin{aligned} L_{aa} &= L_0 - L_2 \cos(2\theta) - L_c \sin(2\theta) \\ L_{bb} &= L_0 - L_2 \cos\left(2\theta + \frac{2\pi}{3}\right) - L_c \sin\left(2\theta + \frac{2\pi}{3}\right) \\ L_{cc} &= L_0 - L_2 \cos\left(2\theta - \frac{2\pi}{3}\right) - L_c \sin\left(2\theta - \frac{2\pi}{3}\right) \\ L_{ab} &= L_{ba} = M_0 - M_2 \cos\left(2\theta - \frac{2\pi}{3}\right) - M_c \sin\left(2\theta - \frac{2\pi}{3}\right) \\ L_{bc} &= L_{cb} = M_0 - M_2 \cos(2\theta) - M_c \sin(2\theta) \\ L_{ac} &= L_{ca} = M_0 - M_2 \cos\left(2\theta + \frac{2\pi}{3}\right) - M_c \sin\left(2\theta + \frac{2\pi}{3}\right), \end{aligned} \quad (24)$$

where  $L_c$  and  $M_c$  are respectively the amplitude of the self and mutual inductances components due to magnetic saturation. Defining the following quantities:

$$\begin{aligned}
L_s &= \sqrt{L_2^2 + L_c^2} \\
M_s &= \sqrt{M_2^2 + M_c^2} \\
\theta_1 &= -\arctan\left(\frac{L_c}{L_2}\right) \\
\theta_2 &= -\arctan\left(\frac{M_c}{M_2}\right), \quad (25)
\end{aligned}$$

the inductances can be written as:

$$\begin{aligned}
L_{aa} &= L_0 - L_s \cos(2\theta + \theta_1) \\
L_{bb} &= L_0 - L_s \cos\left(2\theta + \frac{2\pi}{3} + \theta_1\right) \\
L_{cc} &= L_0 - L_s \cos\left(2\theta - \frac{2\pi}{3} + \theta_1\right) \\
L_{ab} &= L_{ba} = M_0 - M_s \cos\left(2\theta - \frac{2\pi}{3} + \theta_2\right) \\
L_{bc} &= L_{cb} = M_0 - M_s \cos(2\theta + \theta_2) \\
L_{ac} &= L_{ca} = M_0 - M_s \cos\left(2\theta + \frac{2\pi}{3} + \theta_2\right). \quad (26)
\end{aligned}$$

Starting from (26) and using (18) the  $\Gamma_{abc}$  signals can be calculated. Applying the Clarke transformation (19), these signals can be expressed in the  $\alpha\beta\gamma$  reference frame leading to:

$$\begin{aligned}
\Gamma_\alpha &= -[2L_s^2 \cos(4\theta + 2\theta_1) - 4M_s^2 \cos(4\theta + 2\theta_2) \\
&\quad + 2L_s M_s \cos(4\theta + \theta_1 + \theta_2) + 4L_0 L_s \cos(2\theta + \theta_1) \\
&\quad - 4L_s M_0 \cos(2\theta + \theta_1) - 4L_0 M_s \cos(2\theta + \theta_2) \\
&\quad + 4M_0 M_s \cos(2\theta + \theta_2)]/D, \quad (27)
\end{aligned}$$

$$\begin{aligned}
\Gamma_\beta &= -[2L_s^2 \sin(4\theta + 2\theta_1) - 4M_s^2 \sin(4\theta + 2\theta_2) \\
&\quad + 2L_s M_s \sin(4\theta + \theta_1 + \theta_2) - 4L_0 L_s \sin(2\theta + \theta_1) \\
&\quad + 4L_s M_0 \sin(2\theta + \theta_1) + 4L_0 M_s \sin(2\theta + \theta_2) \\
&\quad - 4M_0 M_s \sin(2\theta + \theta_2)]/D, \quad (28)
\end{aligned}$$

$$\Gamma_\gamma = 0, \quad (29)$$

where:

$$\begin{aligned}
D &= 3[-4L_0^2 + 8L_0 M_0 + L_s^2 + 4L_s M_s \cos(\theta_1 - \theta_2) \\
&\quad - 4M_0^2 + 4M_s^2]. \quad (30)
\end{aligned}$$

After some algebraic operations the following quantities can be defined:

$$\begin{aligned}
K_1 &= 2L_s^2 \cos(2\theta_1) - 4M_s^2 \cos(2\theta_2) + 2L_s M_s \cos(\theta_1 + \theta_2) \\
K_2 &= 2L_s^2 \sin(2\theta_1) - 4M_s^2 \sin(2\theta_2) + 2L_s M_s \sin(\theta_1 + \theta_2) \\
K_3 &= 4L_s(L_0 - M_0) \cos(\theta_1) + 4M_s(M_0 - L_0) \cos(\theta_2) \\
K_4 &= 4L_s(L_0 - M_0) \sin(\theta_1) + 4M_s(M_0 - L_0) \sin(\theta_2) \quad (31)
\end{aligned}$$

and then,

$$\begin{aligned}
a &= \sqrt{K_3^2 + K_4^2} \\
b &= \sqrt{K_1^2 + K_2^2} \\
\varphi_a &= \arctan\left(\frac{K_4}{K_3}\right) \\
\varphi_b &= \arctan\left(\frac{K_2}{K_1}\right). \quad (32)
\end{aligned}$$

Thus, (27) and (28) can be written as follows:

$$\begin{aligned}
\Gamma_\alpha &= -a \cos(2\theta + \varphi_a) - b \cos(4\theta + \varphi_b) \\
\Gamma_\beta &= a \sin(2\theta + \varphi_a) - b \sin(4\theta + \varphi_b). \quad (33)
\end{aligned}$$

As shown in [28] and [39], starting from (33), since  $\Gamma_\alpha$  and  $\Gamma_\beta$  are position dependent, the rotor position can be estimated. Let us define the complex number:

$$\hat{\Gamma} = \Gamma_\alpha + j\Gamma_\beta, \quad (34)$$

whose phase  $\chi$  is expressed by (21). In order to extract the electrical rotor position, the DFC angle  $\chi$  of  $\hat{\Gamma}$  can be evaluated. Considering (33) and (34), one can write:

$$\hat{\Gamma} = -ae^{-j(2\theta + \varphi_a)} - be^{j(4\theta + \varphi_b)}. \quad (35)$$

Collecting in (35) the term  $-ae^{-j2\theta}$  leads to:

$$\hat{\Gamma} = -ae^{-j2\theta} \hat{\gamma}, \quad (36)$$

where:

$$\hat{\gamma} = e^{-j\varphi_a} \hat{\gamma}_1, \quad (37)$$

$$\hat{\gamma}_1 = 1 + \frac{b}{a} e^{j(6\theta + \varphi_a + \varphi_b)}. \quad (38)$$

Let us consider the angle  $\angle\hat{\gamma}$ :

$$\angle\hat{\gamma} = -\varphi_a + f(\theta), \quad (39)$$

where:

$$f(\theta) = \angle\hat{\gamma}_1 = \arctan\left(\frac{\frac{b}{a} \sin(6\theta + \varphi_a + \varphi_b)}{1 + \frac{b}{a} \cos(6\theta + \varphi_a + \varphi_b)}\right). \quad (40)$$

Thus,  $\chi = \angle\hat{\Gamma}$  can be written as:

$$\chi = \begin{cases} -2\theta + \pi - \varphi_a + f(\theta), & \text{Re}(\hat{\gamma}_1) \geq 0 \\ -2\theta - \varphi_a + f(\theta), & \text{Re}(\hat{\gamma}_1) < 0 \end{cases}. \quad (41)$$

It is worth noticing that  $\text{Re}(\hat{\gamma}_1) = 1 + \frac{b}{a} \cos(6\theta + \varphi_a + \varphi_b)$ . Therefore,  $\chi$  is twice the electrical rotor position  $\theta$  in the opposite direction plus a phase shift  $\varphi_a$  and a superimposed oscillation  $f(\theta)$ , which is a nonlinear function of the 6th harmonic component of the rotor position and depends on the phase shifts  $\varphi_a$  and  $\varphi_b$  caused by the magnetic saturation effects. Compared to the results presented in [28, 39], the magnetic saturation effects introduce an offset  $\varphi_a$  and a different expression of  $f(\theta)$  which depends on the phase shift caused by these effects on the harmonics of the  $\Gamma_{\alpha\beta\gamma}$  signals. It is important to remark that the angle  $\chi$  can be subject to variation of  $\pi$  in the case  $|\frac{b}{a}| > 1$  due to the conditions on  $\text{Re}(\hat{\gamma}_1)$ . Whereas in the case  $|\frac{b}{a}| \leq 1$  no switching between the two conditions is required. Nevertheless, in low power concentrated windings PMSMs, the amplitude of  $b$  is typically much smaller than the one of  $a$ . Thus, in standard applications, the evaluation of the DFC angle  $\chi$  does not require a switching between the two conditions. Starting from (41), the electrical rotor angle can be obtained as follows:

$$\theta = \begin{cases} \frac{\pi - \chi - \varphi_a + f(\theta)}{2}, & \text{Re}(\hat{\gamma}_1) \geq 0 \\ \frac{-\chi - \varphi_a + f(\theta)}{2}, & \text{Re}(\hat{\gamma}_1) < 0 \end{cases}. \quad (42)$$

Nevertheless, since the effects of magnetic saturation  $\varphi_a$  and of the nonlinear superimposed oscillation  $f(\theta)$  are not known, the estimated electrical rotor position  $\hat{\theta}$  is:

$$\hat{\theta} = \begin{cases} \frac{\pi - \chi}{2}, & \text{Re}(\hat{\gamma}_1) \geq 0 \\ -\frac{\chi}{2}, & \text{Re}(\hat{\gamma}_1) < 0 \end{cases}. \quad (43)$$

Finally, one can define the position estimation error  $\tilde{\theta}$  as:

$$\tilde{\theta} = \theta - \hat{\theta} = \frac{-\varphi_a + f(\theta)}{2}. \quad (44)$$

It has to be remarked that the estimated position given by (43) is the position estimated using the DFC technique when the effects of cross-coupling magnetic saturation are neglected. Therefore, identifying  $\varphi_a$  and compensating for it in (43) is necessary in order to obtain a more reliable estimation of the electrical rotor position in loaded machines. The compensation of this offset with the objective of improving the electrical rotor position estimation is called stator flux compensation. Thus, the expression of the estimated rotor position after this compensation  $\hat{\theta}^*$  results to be:

$$\hat{\theta}^* = \begin{cases} \frac{\pi - \chi}{2} - \frac{\varphi_a}{2}, & \text{Re}(\hat{\gamma}_1) \geq 0 \\ -\frac{\chi}{2} - \frac{\varphi_a}{2}, & \text{Re}(\hat{\gamma}_1) < 0 \end{cases}. \quad (45)$$

**TABLE 1** Expression of  $\varphi_a$  related to the amplitude of the harmonics of the phase inductances

$\varphi_a$	$L_0 < M_0$	$L_0 \geq M_0$
$L_2 < M_2$	$\sigma$	$\sigma + \pi$
$L_2 \geq M_2$	$\sigma + \pi$	$\sigma$

Despite this operation, the presence of the nonlinear oscillation  $f(\theta)$  limited in the range  $\pm \arctan(\frac{b}{a})$  will affect the estimated position. Therefore, after compensating for the offset  $\varphi_a$ , the position error will be equal to:

$$\tilde{\theta}^* = \theta - \hat{\theta}^* = \frac{f(\theta)}{2}. \quad (46)$$

In the following, a more accurate analysis on the offset  $\varphi_a$  on the estimated position introduced by the magnetic saturation effects is reported. From (32) and (31), the following expression can be derived:

$$\varphi_a = \angle[4(L_0 - M_0)(L_s e^{j\theta_1} - M_s e^{j\theta_2})], \quad (47)$$

where:

$$\begin{aligned} \angle(L_s e^{j\theta_1} - M_s e^{j\theta_2}) &= \arctan\left(\frac{L_s \sin(\theta_1) - M_s \sin(\theta_2)}{L_s \cos(\theta_1) - M_s \cos(\theta_2)}\right) \\ &= \arctan\left(\frac{L_c - M_c}{L_2 - M_2}\right) = \sigma. \end{aligned} \quad (48)$$

Therefore, the expression of  $\varphi_a$  in relation to the amplitude of the harmonic components of the phase inductances has been summarised in Table 1. As one can see, the phase shift depends not only on the magnetic saturation but also on the relationship between the amplitude of the continuous component and of the second harmonic of the self and mutual inductances which might add a phase shift of  $\pi$  that must be accounted for.

This mathematical model exhibits differences with respect to the model proposed in [39]. On the one hand, the amplitudes  $a$  and  $b$  of the two harmonic components of the vector  $\Gamma_{\alpha\beta\gamma}$  are current dependent and can change according to the machine stator flux. Moreover, the two harmonic components exhibit phase shift for the second and fourth harmonic of  $\varphi_a$  and  $\varphi_b$ , respectively. Such phase shifts are also stator flux dependent and null at zero stator flux. It is worth noticing that, at zero stator flux, the derived mathematical model of this work is the same as the one previously proposed. Phase shifting of the harmonics has a direct influence on the estimated rotor position. On the one hand, the estimated angle presents an offset due only to the angle  $\varphi_a$ . This angle needs to be compensated for in order to maintain the mean error of the estimated quantity to zero. On the other hand, one can observe that the ripple  $f(\theta)$  affecting the estimated electrical angle undergoes a phase shift of  $\varphi_a + \varphi_b$ .



**TABLE 2** Parameters of the custom PMSM

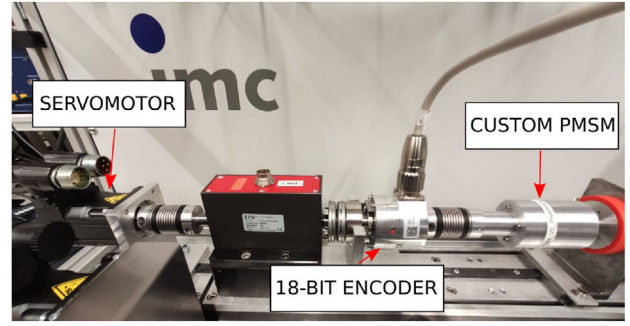
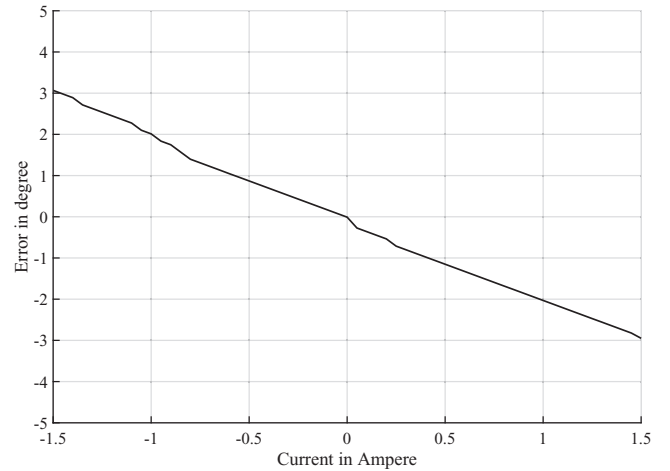
Motor parameters	Values
Phase resistance	1.1 $\Omega$
$d$ -axis inductance	394 $\mu\text{H}$
$q$ -axis inductance	475 $\mu\text{H}$
Pole pairs	8
Torque constant	0.1186 $\frac{\text{Nm}}{\text{A}}$
Nominal voltage	24 V
Nominal current	1.5 A
Nominal speed	500 RPM
Nominal torque	200 mNm

## 4 | EXPERIMENTAL VALIDATION

In the previous sections, an analysis of the DFC technique applied to PMSMs experiencing magnetic saturation has been proposed. As it has been observed, the estimated electrical rotor position is affected by an offset plus a nonlinear oscillation. In this section, the proposed theory has been verified through experimental investigations. In order to verify its validity and the driving capabilities of the DFC technique under different load conditions for low power concentrated windings PMSMs, the following experiments have been conducted. Firstly, the position estimation error caused by the influence of the stator currents has been evaluated in locked rotor conditions. After that, the amplitudes and the phase shifts of the signals  $\Gamma_\alpha$  and  $\Gamma_\beta$  together with the corresponding average rotor position estimation error have been evaluated at different speed and current levels. Finally, the DFC driving capabilities in presence of magnetic saturation have been tested in several dynamic and load conditions.

### 4.1 | Description of the experimental test bench

The motor used for the experimental investigations is a low-power outer rotor PMSMs, whose main parameters are listed in Table 2. The machine has an outer diameter of 42 mm, a stack-length of 30 mm and an airgap of 0.4 mm. Moreover, it is made of 18 stator slots and 16 poles and is equipped with three-phase single layer concentrated windings in star configuration. Also, it presents neodymium (NdFeB) permanent magnets which are 90% embedded into the laminated rotor core. The test bench used for the experimental validations is composed of the custom PMSM coupled to a servo-motor that is used to apply load torques and to a high-precision 18-bit encoder, as shown in Figure 4. In order to drive the motor and perform the necessary measurements, an electronic board featuring a 32-bit microcontroller, a three-phase inverter and the sensing circuitry has been developed. Moreover, in order to measure the star-point voltage of the electrical machine accurately, a dedicated electronics implementing direct voltage measurement (DVM) shown in [28] has been used.

**FIGURE 4** Test bench used for experimental validation**FIGURE 5** Measured position estimation error as a function of the  $q$ -axis current under locked rotor conditions

### 4.2 | Evaluation of the error due to magnetic saturation under locked rotor conditions

In the first experiment, the error on the rotor position estimation introduced by magnetic saturation effects under locked rotor conditions at different current levels has been analysed. The motor has been locked to zero degrees and controlled in current using a standard field oriented control (FOC) technique based on the encoder mounted in the test bench. In particular, the  $q$ -axis current has been driven within its nominal range  $\pm 1.5\text{A}$  and the resulting error in the DFC estimated position has been reported in Figure 5. From (44), the resulting position error in locked rotor condition is equal to:

$$\tilde{\theta}|_{\theta=0} = \frac{-\varphi_a + f(0)}{2}, \quad (49)$$

where:

$$f(0) = \arctan \left( \frac{\frac{b}{a} \sin(\varphi_a + \varphi_b)}{1 + \frac{b}{a} \cos(\varphi_a + \varphi_b)} \right). \quad (50)$$

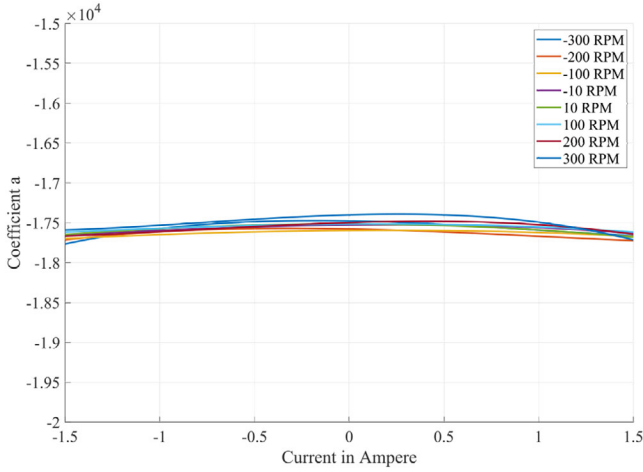


FIGURE 6 Coefficient  $a$  at different current and speed levels

From equation (49) and (50), one can observe that the position estimation error  $\tilde{\theta}$  in locked rotor conditions is related to the saturation level of the machine since it depends on the values of  $a$ ,  $b$ ,  $\varphi_a$  and  $\varphi_b$ . It can be easily observed that in absence of stator currents  $\tilde{\theta}|_{\theta=0} = 0$  since  $\varphi_a = \varphi_b = 0$ . From Figure 5, one can observe that the position estimation error  $\tilde{\theta}$  under locked rotor conditions is limited in the range  $\pm 3^\circ$  and its dependence on the  $q$ -axis current is almost linear. Also, it can be observed that the position error results to be equal to zero in absence of stator currents.

### 4.3 | Evaluation of the error due to magnetic saturation under dynamic conditions

In order to validate the proposed mathematical model, a frequency analysis of the signals  $\Gamma_\alpha$  and  $\Gamma_\beta$  together with the evaluation of the average rotor position estimation error at different current and speed levels has been carried out. The motor under test has been driven at different speeds within its nominal range ( $\pm 300$  RPM) via the coupled servo-motor and the  $q$ -axis current has been controlled with a standard FOC within  $\pm 1.5$  A using the position information given by the high-resolution encoder. Considering (33), the amplitudes ( $a$  and  $b$ ) and the phase shifts ( $\varphi_a$  and  $\varphi_b$ ) of the main harmonic components of  $\Gamma_\alpha$  and  $\Gamma_\beta$  have been calculated by means of a fast Fourier transform (FFT). In Figure 6, the values of the amplitude of the 2nd harmonics  $a$  at different currents and speeds are reported. In Figure 7, the profile of the amplitude of the 4th harmonics  $b$  at different currents and speeds is shown. As one can notice, for both coefficients the percentage variation with respect to currents and speeds is small. In fact, the maximum variation for the coefficient  $a$  is 1.13%, while for the coefficient  $b$  is 2.33%. In addition, their mean values are respectively  $\bar{a} = -17568$  and  $\bar{b} = -2207.4$  expressed in ADC ticks. Figures 8 and 9 report the profile of the phase shifts of the 2nd and 4th harmonics  $\varphi_a$  and  $\varphi_b$  respectively at different current and speed levels. One can notice that both the phase shifts vary almost linearly with

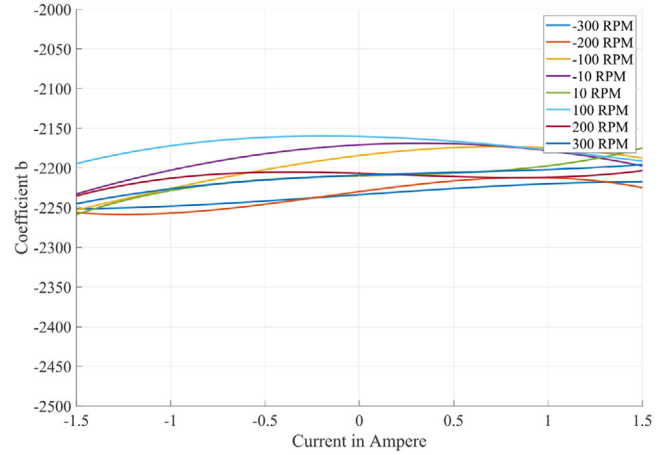


FIGURE 7 Coefficient  $b$  at different current and speed levels

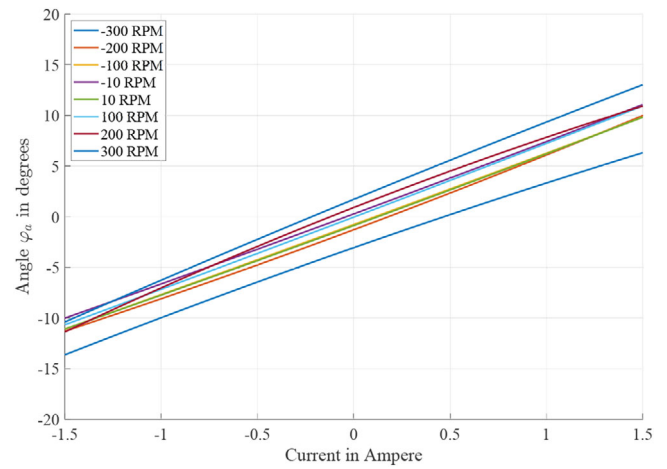


FIGURE 8 Phase shift  $\varphi_a$  at different current and speed levels

respect to current and speed variations. Also, from this analysis it results that the maximum range of variation of the coefficients  $\varphi_a$  and  $\varphi_b$  is respectively  $\varphi_a \in [-13.64^\circ; 13.02^\circ]$  and  $\varphi_b \in [-26.83^\circ; 29.05^\circ]$ . Moreover, it can be seen that the coefficients present a variability at the same stator current level due to the effects of the rotor speed. In particular, the maximum variation range over the mean value at the same current level of the coefficients  $\varphi_a$  and  $\varphi_b$  is respectively  $\pm 3.35^\circ$  and  $\pm 5.6^\circ$ . In Figure 10, the average rotor position estimation error at different current and speed levels has been reported. Under dynamic conditions the instantaneous position estimation error is given by (44). It has to be remarked that there is an additional position error caused by the effects of rotor speed due to the sequential acquisition of the  $\Gamma_{\alpha\beta\gamma}$  signals. Since in absence of stator currents  $\varphi_a = \varphi_b = 0$ , the expression of the position error under dynamic and no load conditions is:

$$\tilde{\theta}|_{i_{abc}=0} = \frac{f(\theta)|_{i_{abc}=0}}{2}, \quad (51)$$

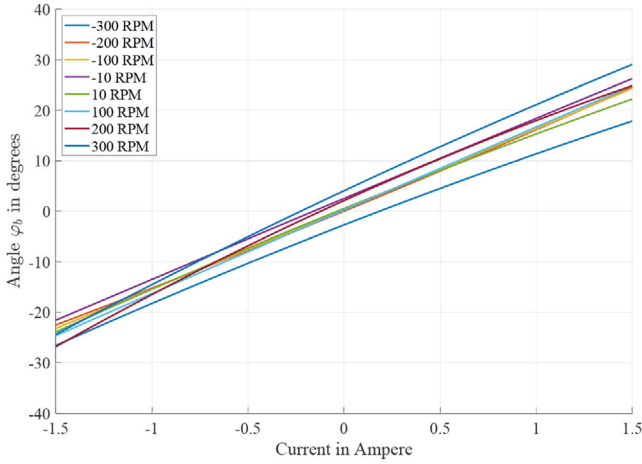


FIGURE 9 Phase shift  $\varphi_b$  at different current and speed levels

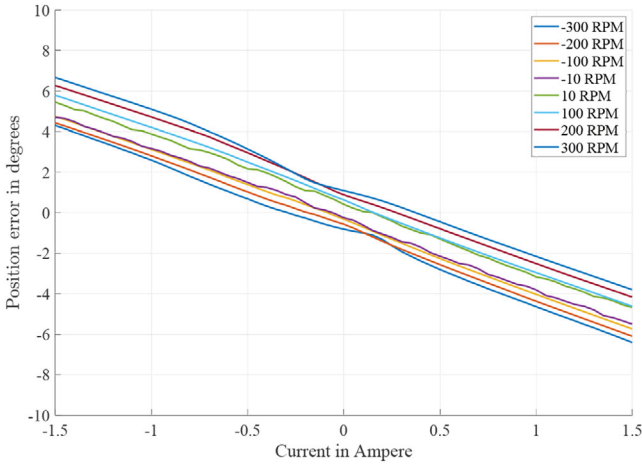


FIGURE 10 Average position estimation error at different current and speed levels

where:

$$f(\theta)|_{i_{abc}=0} = \arctan\left(\frac{\frac{b}{a} \sin 6\theta}{1 + \frac{b}{a} \cos 6\theta}\right). \quad (52)$$

Nevertheless, it has to be remarked that the average value of the position error has been calculated considering an integer number of periods of the  $\Gamma_{\alpha\beta\gamma}$  signals. Therefore, under these hypotheses the effect of  $f(\theta)$  on the average position error is negligible, since its average value is zero. Thus, at zero current the only effect which affects the average position estimation error is the error caused by the rotor speed during the acquisition of the anisotropy signals. The maximum average position error at zero current due to the effects of the rotor speed is equal to  $1.09^\circ$  at 300 RPM. As it can be observed this error increases with the rotor speed. Moreover, one can notice that the average position error increases with the stator current level. In particu-

lar, this average position error  $\bar{\theta}$  results to be:

$$\bar{\theta} = \frac{-\varphi_a + \bar{f}(\theta)}{2} = -\frac{\varphi_a}{2}. \quad (53)$$

One can conclude that the average position error under dynamic conditions is described by (53) when the effects of the rotor speed are neglected, since the average value of the nonlinear oscillation  $\bar{f}(\theta)$  is equal to zero. It can be observed that under dynamic conditions, the average position error  $\bar{\theta}$  is limited in the range  $[-6.41^\circ; 6.68^\circ]$ . This range results to be bigger than the one obtained in locked rotor condition due to the different expression of (49) and (53) and to the effects of rotor speed. Moreover, at a fixed current level the maximum range of variability over the mean value of the average position estimation error is  $\pm 1.19^\circ$ . This variability represents the error introduced by the rotor speed at a fixed stator current.

The conducted identification procedure validates the proposed model, showing that the parameters characterizing the vector  $\Gamma_{\alpha\beta\gamma}$ , namely  $a$ ,  $b$ ,  $\varphi_a$  and  $\varphi_b$ , are current dependent. Also, the angles  $\varphi_a$  and  $\varphi_b$  are null at zero current when the effects of rotor speed are negligible. The identified parameters can then be used to perform stator flux compensation and to adjust the mean error of the estimated electrical rotor position.

#### 4.4 | Evaluation of motor driving capabilities using the DFC technique

The identification of the parameters of the DFC signals  $\Gamma_{\alpha\beta\gamma}$  of the electrical machine under test not only validates the proposed mathematical model but can be used for performing stator flux compensation when driving the machine under loaded conditions. As shown by the mathematical model, the angle  $\varphi_a$  is responsible of a position error in the electrical position estimation and it is a function of  $q$ -axis current. By considering the acquired data in the previous experiment, a simple polynomial model has been identified and used for correcting the DFC angle. Two different tests have been conducted. In the first experiment, the PMSM under test has been controlled up to its nominal speed of 300 RPM in both directions by means of FOC at two different load conditions. Figure 11 shows the results obtained when the machine is unloaded, while in Figure 12 the performance obtained with a fully loaded machine is presented, with the load being 200 mNm. In both experiments, stator flux compensation has been applied to the estimated electrical rotor angle and this quantity has been used for controlling the machine. In both figures, the speed profile is shown and compared to the speed measured by means of DFC and by means of the encoder. As one can observe, the DFC speed exhibits oscillations. This is due to the presence of the DFC ripple ( $f(\theta)$ ). Nevertheless, the presence of oscillations does not affect the performance of the speed controller, as confirmed by the encoder speed that provides the real speed of the machine and that does not exhibit oscillations. This is coherent with low-pass filter behaviour of the chosen speed

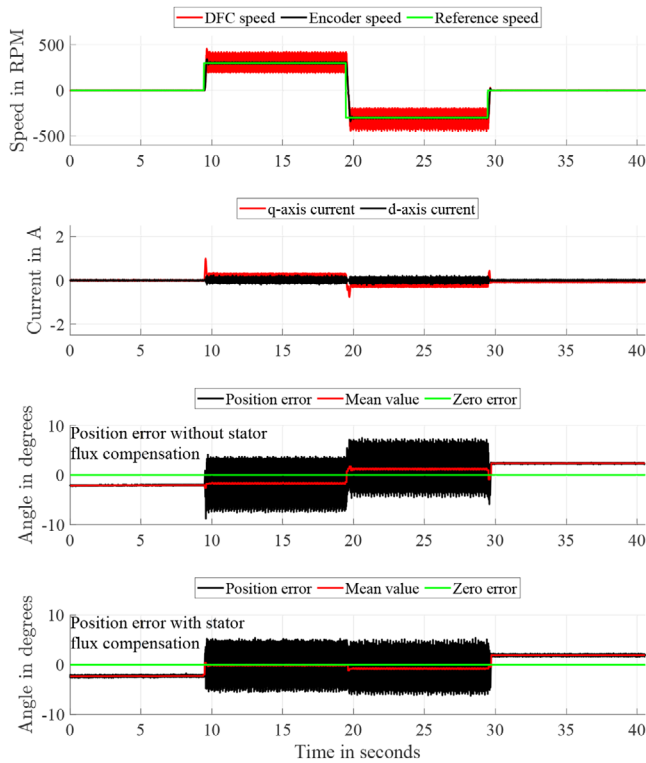


**FIGURE 11** Motor speed control under no load conditions. From top to bottom: Comparison between DFC, encoder and reference speed. Currents of  $d$  and  $q$  axes. Position error and corresponding mean value without and with stator flux compensation

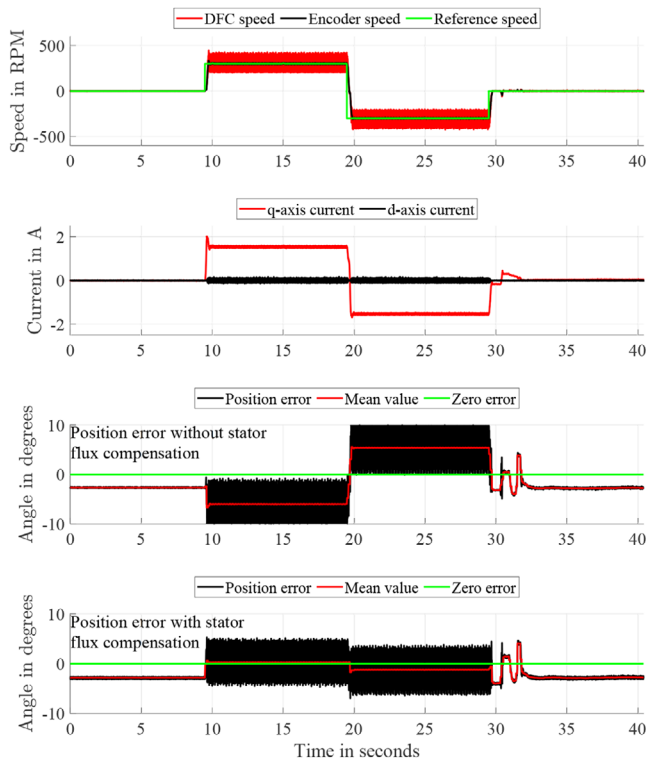


**FIGURE 12** Motor speed control with nominal load applied. From top to bottom: Comparison between DFC, encoder and reference speed. Currents of  $d$  and  $q$  axes. Position error and corresponding mean value without and with stator flux compensation

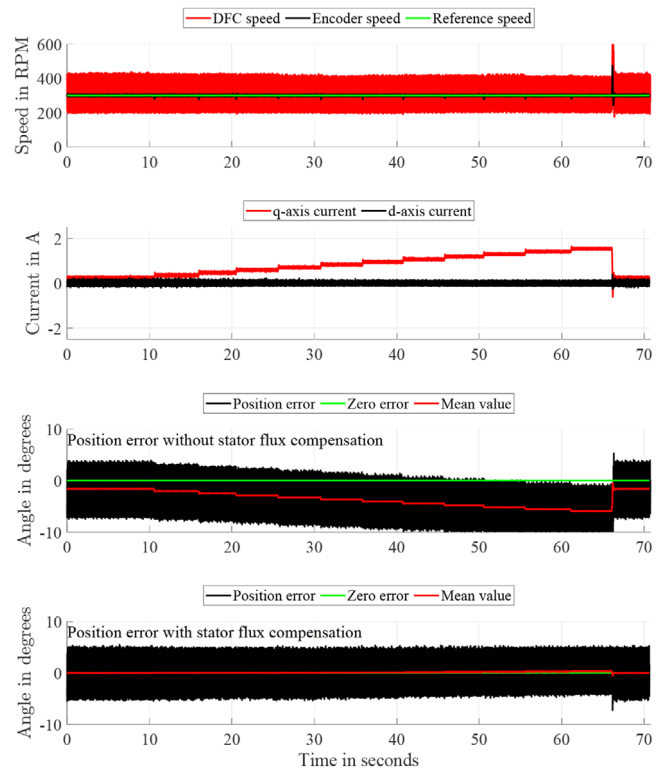


**FIGURE 13** Motor speed control with increasing loads applied. From top to bottom: Comparison between DFC, encoder and reference speed. Currents of  $d$  and  $q$  axes. Position error and corresponding mean value without and with stator flux compensation

controller. Moreover, the stator currents controlled along the  $d$ - and the  $q$ - axis are shown, where the  $d$ -axis current is controlled to zero to avoid defluxing the rotor. Finally, the position error obtained by the DFC technique is shown before and after applying stator flux compensation. The position error is oscillating due to the DFC ripple  $f(\theta)$  that is a harmonic signal with zero mean value. As one can notice, the amplitude of the DFC ripple stays constant since it depends on the coefficients  $a$  and  $b$  that do not vary significantly over current and speed as shown in the previous section. Nevertheless, the mean value of the position error shows dependency on the current, as expected by the model. By performing stator flux compensation, the mean value can be minimised as much as the precision provided by the identified model of the quantity  $\varphi_a$ . In particular, in Figure 11 the maximum average position error in the speed control is equal to  $-1.5^\circ$  at 0.3 A, whereas in Figure 12 the maximum average position error in the speed control results  $-6.1^\circ$  at 1.5 A. These results agree with the ones obtained in Figure 10. After the stator flux compensation, the maximum average position error in the speed control at the same current levels is respectively  $-0.9^\circ$  in absence (Figure 11) and  $-1.2^\circ$  in presence (Figure 12) of an applied load. One can conclude that the stator-flux compensation improves the position estimation since the average position error is significantly reduced and close to zero. In fact, the reduction of the average position error is respectively about 43% in absence and 82% in presence of an



applied load. The remaining average position error is due to the effects of the rotor speed.

In the second experiment, the motor has been controlled at its nominal speed of 300 RPM by using again an FOC controller based on the DFC angle after stator flux compensation has been applied. Once the rotor has achieved nominal speed, several increasing load torques have been progressively applied in order to highlight the disturbance rejection capabilities when controlling the machine with star-point voltage based sensorless techniques. In Figure 13, one can observe the increasing load on the machine by observing the demanded  $q$ -axis current of the controller, that reaches its nominal value of 1.5 A. Also in this case, one can observe how the position error increases consistently with the stator current. In particular, the average position error at 1.5 A is equal to  $-6^\circ$  in accordance with the results shown in Figure 10. By applying stator flux compensation, instead, the mean value of the estimated electrical rotor angle is  $0.3^\circ$  at 1.5 A. Also in this experiment, one can observe that the stator flux compensation reduces the average position estimation error and the remaining error is related to the effects of the rotor speed. In this case, the reduction of the average position error after the stator flux compensation is about 95%.

## 5 | CONCLUSIONS AND OUTLOOKS

In this work the effects of magnetic saturation on star-point voltage exploiting techniques have been analysed and evaluated leading to a method for performing stator flux compensation. In particular, the influence of stator currents on the estimated rotor position obtained with the DFC technique has been analysed. This technique is an anisotropy based technique which estimates the rotor position starting from zero-sequence voltage measurements. While for several common HFI techniques, which rely on current measurements, the effects of magnetic saturation on the estimated position are well known in literature, the possibility of driving heavy loaded machines which exploit the star-point voltage information has been analysed in this work. Considering a symmetric inductances matrix which takes into account the presence of magnetic saturation effects, a new expression of the  $\Gamma_{\alpha\beta\gamma}$  has been derived. This analysis has shown that the magnetic saturation determines a phase shift of the DFC signals on all their harmonic components and therefore an offset on the estimated rotor position plus a nonlinear oscillation which is a function of the rotor position and of the stator currents. Thus, for machines operating under load, a compensation of this offset is mandatory to obtain a more reliable position information. The obtained mathematical results have been then validated through experimental tests using a custom PMSM. Firstly, the position error has been evaluated in locked rotor conditions. The experiment has confirmed that the stator currents introduce an offset on the estimated position. After that, the effects of magnetic saturation have been evaluated. By means of frequency analysis, the coefficients of the vector  $\Gamma_{\alpha\beta\gamma}$  have been evaluated showing an almost linear dependence of the phase shifts on the stator currents level. Under these conditions, the average estimated position error has been analysed

showing its dependence on both current and speed. Finally, the driving capabilities of the DFC technique in trajectory tracking and disturbance rejection applications in presence of magnetic saturation effects have been tested by performing stator flux compensation. The results of this work show that reliable sensorless operation can be obtained using star-point voltage based sensorless techniques also in presence of magnetic saturation. Nevertheless, a nonlinear oscillation on the estimated position is still present. Therefore, in future works, in order to reduce this effect, techniques capable of compensating for the position error will be investigated. In addition, the effects of asymmetries and of higher harmonics on the inductances matrix will be analysed and validated through field distribution simulations in order to increase the accuracy of the proposed model.

## Acknowledgement

We acknowledge support by the Deutsche Forschungsgemeinschaft (DFG, German Research Foundation) and Saarland University within the funding programme Open Access Publishing.

## ORCID

Emanuele Grasso  <https://orcid.org/0000-0003-4723-3381>

Marco Palmieri  <https://orcid.org/0000-0003-2598-773X>

## REFERENCES

1. Yang, Z., et al.: Comparative study of interior permanent magnet, induction, and switched reluctance motor drives for EV and HEV applications. *IEEE Trans. Transp. Electrification*. 1(3), 245–254 (2015)
2. Xu, D., et al.: A review of sensorless control methods for AC motor drives. *CES Trans. Electr. Mach. Syst.* 2(1), 104–115 (2018)
3. Schrödl, M.: Sensorless Control of A. C. Machines; Fortschritt-Berichte VDI: Reihe 21, Elektrotechnik; Volume 117 (1992)
4. Schrödl, M.: Sensorless control of AC machines at low speed and standstill based on the “INFORM” method. In: Proceedings of the IAS '96. Conference Record of the 1996 IEEE Industry Applications Conference Thirty-First IAS Annual Meeting, pp. 270–277. IEEE, Piscataway, NJ (1996)
5. Lorenz, R.D.: Transducerless position and velocity estimation in induction and salient AC machines. *IEEE Trans. Ind. Appl.* 31(2), 240–247 (1995)
6. Corley, M., Lorenz, R.: Rotor position and velocity estimation for a salient-pole permanent magnet synchronous machine at standstill and high speeds. *IEEE Trans. Ind. Appl.* 34(4), 784–789 (1998)
7. Linke, M., Kennel, R., Holtz, J.: Sensorless position control of permanent magnet synchronous machines without limitation at zero speed. In: Proceedings of the IEEE 2002 28th Annual Conference of the Industrial Electronics, pp. 674–679. IEEE, Piscataway, NJ (2002)
8. Linke, M., Kennel, R., Holtz, J.: Sensorless speed and position control of synchronous machines using alternating carrier injection. In: Proceedings of the IEEE International Electric Machines and Drives, pp. 1211–1217. IEEE, Piscataway, NJ (2003)
9. Landsmann, P., et al.: Saliency based encoderless predictive torque control without signal injection. In: Proceedings of the 2010 International Power Electronics, pp. 3029–3034. IEEE, Piscataway, NJ (2010)
10. Paulus, D., Landsmann, P., Kennel, R.: Sensorless field-oriented control for permanent magnet synchronous machines with an arbitrary injection scheme and direct angle calculation. In: Proceedings of the 2011 Symposium on Sensorless Control for Electrical, pp. 41–46. IEEE, Piscataway, NJ (2011)
11. Paulus, D., Landsmann, P., Kennel, R.: Saliency based sensorless field-oriented control for permanent magnet synchronous machines in the whole speed range. In: Proceedings of the 3rd IEEE International Symposium on Sensorless Control for Electrical, pp. 1–6. IEEE, Piscataway, NJ (2012)



12. Landsmann, P.: Sensorless control of synchronous machines by linear approximation of oversampled current. Dissertation, Technical University of Munich, Munich (2014)
13. Consoli, A., Scarcella, G., Testa, A.: A new zero-frequency flux-position detection approach for direct-field-oriented-control drives. *IEEE Trans. Ind. Appl.* 36, 797–804 (2000)
14. Consoli, A., et al.: Air-gap flux position estimation of inaccessible neutral induction machines by zero-sequence voltage. *Electr. Power Components Syst.* 30, 7–88 (2002)
15. Holtz, J., Pan, H.: Elimination of saturation effects in sensorless position controlled induction motors. In: Proceedings of the Conference Record of the 2002 IEEE Industry Applications Conference. 37th IAS Annual Meeting pp. 1695–1702. IEEE, Piscataway, NJ (2002)
16. Holtz, J., Pan, H.: Acquisition of Rotor Anisotropy Signals in Sensorless Position Control Systems. *IEEE Trans. Ind. Appl.* 40, 1379–1387 (2004)
17. Holtz, J.: Sensorless Control of Induction Machines—With or Without Signal Injection? *IEEE Trans. Ind. Electron.* 53, 7–30 (2006)
18. Consoli, A., et al.: Zero frequency rotor position detection for synchronous PM motors. In: Proceedings of the 2000 IEEE 31st Annual Power Electronics Specialists Conference. pp. 879–884. IEEE, Piscataway, NJ (2000)
19. Strothmann, R.: Fremderregte Elektrische Maschine. EP1005716B1, 14 November 2001
20. Thiemann, P., et al.: Direct Flux Control (DFC): A New Sensorless Control Method for PMSM. In: Proceedings of the 2011 46th International Universities' Power Engineering Conference, pp. 1–6. IEEE, Piscataway, NJ (2011)
21. Mantala, C.: Sensorless control of brushless permanent magnet motors. Ph.D. Thesis, University of Bolton, Bolton (2013)
22. Kleen, S., Nienhaus, M.: Simulation and analysis of the winding inductances of small electrical motors for a sensorless control method. In: Proceedings of IKMT, Köln (2015)
23. Kleen, S., Nienhaus, M.: Impact of the embedding of magnets on a sensorless drive method. In: Proceedings of IKMT, Köln (2017)
24. Grasso, E., Kanapari, E., Nienhaus, M.: Analysis of direct flux observation for field oriented control PMSM. In: Proceedings of IKMT, Köln (2015)
25. Grasso, E., Merl, D., Nienhaus, M.: A novel online phase inductance measurement technique for sensorless control applications. In: Proceedings of the ACTUATOR 2014, Messe Bremen, Bremen (2014)
26. Grasso, E., Merl, D., Nienhaus, M.: Verfahren und Vorrichtung zum Bestimmen einer Läuferlage eines Läufers einer elektronisch kommutierten elektrischen Maschine. DE DE102016117258A1 (21 March 2018)
27. Merl, D., et al.: A direct flux observer based on a fast resettable integrator circuitry for sensorless control of PMSMs. In: Proceedings of the ACTUATOR 2018: 16th International Conference on New Actuators, In: Proceedings of the ACTUATOR 2016. Messe Bremen, Bremen (2018)
28. Grasso, E., Mandriota, R., König, N., Nienhaus, M.: Analysis and Exploitation of the Star-Point Voltage of Synchronous Machines for Sensorless Operation. *Energies* 12(24), 4729 (2019)
29. Grasso, E., et al.: A direct flux observer for robust to noise sensorless control of PMSMs. In: Proceedings of the ACTUATOR 2016. Messe Bremen, Bremen (2018)
30. Fabbri, S., et al.: Full speed range sensorless control for PMSM using an adaptive extended Kalman filter. In: 2020 AEIT International Annual Conference, pp. 1–6. IEEE, Piscataway, NJ (2020)
31. König, N., et al.: Parameter identification of star-connected PMSMs by means of a sensorless technique. In: 2018 Thirteenth International Conference on Ecological Vehicles and Renewable Energies, pp. 1–7. IEEE, Piscataway, NJ (2018)
32. Fabbri, S., et al.: Performance comparison of different estimation techniques of the external load-torque applied on a PMSM using direct flux control. 2020 International Symposium on Power Electronics, Electrical Drives, Automation and Motion, pp. 688–693. IEEE, Piscataway, NJ (2020)
33. Iwaji, Y., Kokami, Y., Kurosawa, M.: Position-sensorless control method at low speed for permanent magnet synchronous motors using induced voltage caused by magnetic saturation. In: Proceedings of the 2010 International Power Electronics Conference, pp. 2238–2243. IEEE, Piscataway, NJ (2010)
34. Iwaji, Y., et al.: Position sensorless control method at zero-speed region for permanent magnet synchronous motors using the neutral point voltage of stator windings. *IEEE Trans. Ind. Appl.* 52, 4020–4028 (2016)
35. Hara, T., et al.: Neutral point voltage model of stator windings of permanent magnet synchronous motors with magnetic asymmetry. In: Proceedings of the 2018 XIII International Conference on Electrical Machines, pp. 1611–1616. IEEE, Piscataway, NJ (2018)
36. Xu, P., Zhu, Z.: Novel carrier signal injection method using zero sequence voltage for sensorless control of PMSM drives. *IEEE Trans. Ind. Electron.* 63(4), (2016)
37. Xu, P.L., Zhu, Z.Q.: Novel square-wave signal injection method using zero-sequence voltage for sensorless control of PMSM drives. *IEEE Trans. Ind. Electron.* 63, 7444–7454 (2016)
38. Schuhmacher, K., Grasso, E., Nienhaus, M.: Improved rotor position determination for a sensorless star-connected PMSM drive using direct flux control. *J. Eng.* 2019(17), 3749–3753 (2019)
39. Grasso, E., et al.: Analysis and application of the direct flux control sensorless technique to low-power PMSMs. *Energies* 13, 1453 (2020)
40. Schuhmacher, K., Kleen, S., Nienhaus, M.: Comparison of anisotropy signals for sensorless control of star-connected PMSMs. In: Proceedings of the 2019 IEEE 10th International Symposium on Sensorless Control for Electrical Drives, pp. 1–6. IEEE, Piscataway, NJ (2019)
41. Yan, Y., et al.: Study of a PMSM model incorporating structural and saturation saliencies. 2005 International Conference on Power Electronics and Drives Systems, pp. 575–580. IEEE, Piscataway, NJ (2005)
42. Raja, R., Sebastian, T., Wang, M.: Online stator inductance estimation for permanent magnet motors using PWM excitation. *IEEE Trans. Transp. Electr.* 5, 107–117 (2019)
43. Poltschak, F., Amrhein, W.: Influence of winding layout of PMSM on inductance and its impact on suitability for sensorless vector control. In: Proceedings of the SPEEDAM, pp. 1002–1007. IEEE, Piscataway, NJ (2010)
44. Farshadnia, M., et al.: Detailed analytical modelling of fractional-slot concentrated-wound interior permanent magnet machines for prediction of torque ripple. In: 2016 IEEE Energy Conversion Congress and Exposition, pp. 1–8. IEEE, Piscataway, NJ (2016)
45. Arellano-Padilla, J., Gerada, C., Asher, G., Sumner, M.: Inductance characteristics of PMSMs and their impact on saliency-based sensorless control. In: Proceedings of 14th International Power Electronics and Motion Control Conference, pp. S1-1–S1-9. IEEE, Piscataway, NJ (2010)
46. Lim, M., Chai, S., Hong, J.: Design of saliency-based sensorless-controlled IPMSM with concentrated winding for EV traction. *IEEE Transactions on Magnetics* 52(3), 1–4 (2016)
47. Chai, S., et al.: Design of IPMSM having high power density for position sensorless operation with high-frequency signal injection and the method of calculating inductance profile. In: 2011 International Conference on Electrical Machines and Systems, pp. 1–5. IEEE, Piscataway, NJ (2011)
48. Gao, Y., Qu, R., Li, D.: Improved hybrid method to calculate inductances of permanent magnet synchronous machines with skewed stators based on winding function theory. *Chinese J. Electr. Eng.* 2(1), 52–61 (2016)

**How to cite this article:** Grasso E, Palmieri M, Mandriota R, Gallicchio G, Cupertino F, Nienhaus M. Influence and compensation of the stator flux on the direct flux control sensorless technique for PMSMs. *J. Eng.* 2021;2021:334–347.  
<https://doi.org/10.1049/tje.2.12039>